Available online at www.sciencedirect.com
ScienceDirect
Electrochimica Acta 51 (2006) 6521–6526
ELECTROCHIMICA Acta
www.elsevier.com/locate/electacta

Investigation of the effect of impingement angle on tribocorrosion using single impacts

Andrew Jonathan Smith, Martin Stratmann [1], Achim Walter Hassel [*,1]

Max-Planck-Institut für Eisenforschung, Düsseldorf, Germany

Received 23 January 2006; received in revised form 25 April 2006; accepted 25 April 2006
Available online 6 June 2006

Dedicated to Prof. Masahiro Seo on occasion of his retirement from Hokkaido University.

Abstract

Using highly sensitive measurement and analog digital conversion devices it was possible to detect the repassivation transients after particle impingement on aluminium. Simultaneous use of a newly constructed slurry-jet and μ-electrodes as targets allowed the highly reproducible detection of single-particle impacts. This, in turn, allowed correlating the charge consumed during repassivation in a potentiostatic experiment with the damage caused. Variation of the experimental geometry allowed tuning the impingement angle to predetermined values. Current transients and the craters resulting from the particle impact were analyzed for impingement angles between 30° and 90°. It was found that both peak current and charge increase with decreasing angle. As a result of the nano-roughness of the impacting zirconia particles used it was possible to ascribe the crater morphologies to the different mechanisms of indentation and scratching. A model that links the normal and lateral components of the kinetic energy to these two wear mechanisms is proposed.
© 2006 Elsevier Ltd. All rights reserved.

Keywords: Tribocorrosion; Particle induced flow corrosion; Passivity; Transients

1. Introduction

The current trend in industrial processes to ever higher flow rates in order to maximize productivity leads to ever higher demands on the materials employed. Especially components subjected to liquid flows containing solid particles show high wear rates. This wear is classified as erosion–corrosion. In erosion–corrosion the synergistic effects of physical abrasion and electrochemical corrosion lead to higher material degradation than the mere sum of both these effects.

Many different approaches to the investigation of tribocorrosion are possible. The most common methods were reviewed by Landolt et al. [1,2]. The tribological contact can be of various natures: sliding, fretting, rolling or impingement. Also the effect of 2-body erosion–corrosion and 3-body erosion–corrosion – with an added abrasive – are discussed.

Another 2-body method is described by Assi and Böhni in [3]. In this approach the use of micro-electrochemical techniques is applied to a tribological system.

The method employed in this work was slurry-jet impingement using slurries of different concentrations. Many groups have been investigating the effects of slurry-erosion, mostly utilizing various kinds of sandblasting tests and performing weight loss measurements using different impingement angles [4–7]. The effects of slurry impingement have been investigated and discussed in more detail in various publications including the works of Zu, Burstein and Li [8–10].

As the method was ever more refined the detection of single impacts became desirable in order to better understand the mechanism of erosion–corrosion during each event. Burstein and Sasaki approached this problem using an acoustic emission sensor [11]. Their results from impingement of silica sand onto stainless steel samples showed that a minimum threshold energy must be overcome in order to depassivate the sample surface. They found that this energy is a function of the impacting particle geometry and the particle momentum. Additionally they found that higher impact energies are required for depassivation at lower impact angles.

* Corresponding author. Tel.: +49 211 6792 464; fax: +49 211 6792 218.
E-mail address: hassel@elchem.de (A.W. Hassel).
[1] ISE active member.

0013-4686/$ – see front matter © 2006 Elsevier Ltd. All rights reserved.
doi:10.1016/j.electacta.2006.04.049

In this work the detection of single-particle impacts is achieved by a reduction in sample size and erodent particle concentration. In order to investigate single impacts it is necessary to reduce the electrode size. By doing this and by using a very small amount of impacting particles the probability of an impact becomes sufficiently low. In this manner it is possible to correlate the recorded current transient with the physical damage to the sample which is assessed by *ex-situ* SEM investigations.

An important factor in investigating tribocorrosion is the knowledge of the repassivation kinetics. How does the passive, corrosion resistant material respond to a rupture of the passivating layer? These questions which were already addressed in the works of Burstein and Davenport and Frankel et al. [12,13] shall be revisited here in the light of single-particle impingement.

2. Experimental

The electrodes used in these experiments were μ-disc electrodes prepared from Al (99.99%, Goodfellow) wires with a diameter of 125 μm. These wires were embedded in glass capillaries using epoxy resin. The capillaries were drawn and ground so that the tips were of the same diameter as the wires giving a smoother electrolyte flow in the experiments described below. Counter electrodes consisted of Au (99.999% Wieland Dentaltechnik) wires with a diameter of 200 μm which were wrapped around the capillaries in the shape of a spiral. For ease of handling and in order to be mounted to the slurry-jet chamber the capillaries were then fixed to cut-off Pasteur pipettes using a thermoplastic polymer.

The samples were electropolished prior to the experiments using a mixture of $HClO_4$ and CH_3COOH (22:78) for 60 s at 20 V at room temperature.

The slurry-jet consists of an acrylic, cube-shaped chamber set on a corner. The nozzle (made from a Pasteur pipette) and the sample are mounted to facing walls of the chamber—this set-up gives an impingement angle of 90° for flat samples. Different impingement geometries were realized by grinding the samples at different angles (Fig. 1). Using this technique enabled the actual sample mounting to be stationary, yielding a more rigid set-up. As the schematic in Fig. 1 (lower part) shows, grinding the samples at different angles causes an increase in surface area. Using Eq. (1) it is possible to derive the surface area from the wire diameter a and the grinding angle α. Table 1 gives the electrode sizes and the differences in electrode size for the angles chosen in this work:

Table 1
Sample surface area as a function of grinding angle

Angle/°	$A/\mu m^2$	$\Delta A/\mu m^2$	%
90	12272	0	0
60	14170	1898	15
45	17355	5083	41
30	24544	12272	100

$$A_{\text{electrode}} = \frac{\pi}{4} a \frac{a}{\sin\alpha} \quad (1)$$

A high-speed pump is used to accelerate the electrolyte (0.1 M acetate buffer, pH 6.0) from the reservoir. The lower tip of the cube acts as a drain. By mounting the nozzle to an x–y-stage it is possible to aim the electrolyte/slurry flow at the sample. A reference electrode ($Hg/HgI_2(OOCCH_3)_2$) is connected via a Luggin capillary. This electrode operates with the same electrolyte that is used in the experiments preventing diffusion potentials. By applying an adjustable siphon to the drain the electrolyte level in the chamber can be precisely adjusted (Fig. 2).

In order to obtain detailed information of the fast repassivation process it is necessary to use high data acquisition rates. For this purpose a high-speed potentiostat with a high bandwidth was used. The employed potentiostat also has a FAst Current

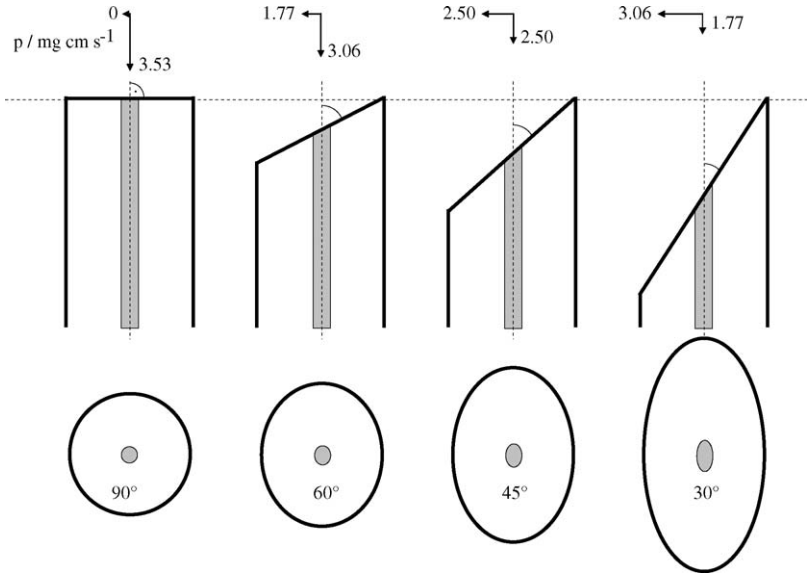

Fig. 1. Samples ground at different angles yield different surface areas as well as different impingement angles. Normal and lateral components of the impulse are given in the headline of the figure.

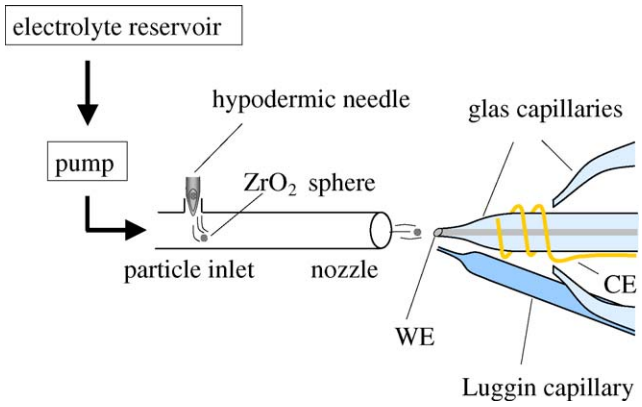

Fig. 2. Schematic of the slurry-jet impingement system.

CONverter (FACCON) which converts the current information into current-equivalent potentials. Furthermore a high-speed analog–digital converter (ADC) was used so that the acquired transient data could be logged on a computer with a data rate of 1 MHz [14].

The abrasive particles used in these experiments were ZrO_2 spheres with a nominal diameter of 125 μm (Fig. 3). In order to introduce a well-defined number of spheres to the system a particle inlet was constructed: a Plexiglas holder was fitted with a main channel through which the electrolyte flows and a small perpendicular loading channel through which the spheres were introduced to the system using a hypodermic needle. Prior to loading the spheres were placed on the tip of the needle and counted under a microscope.

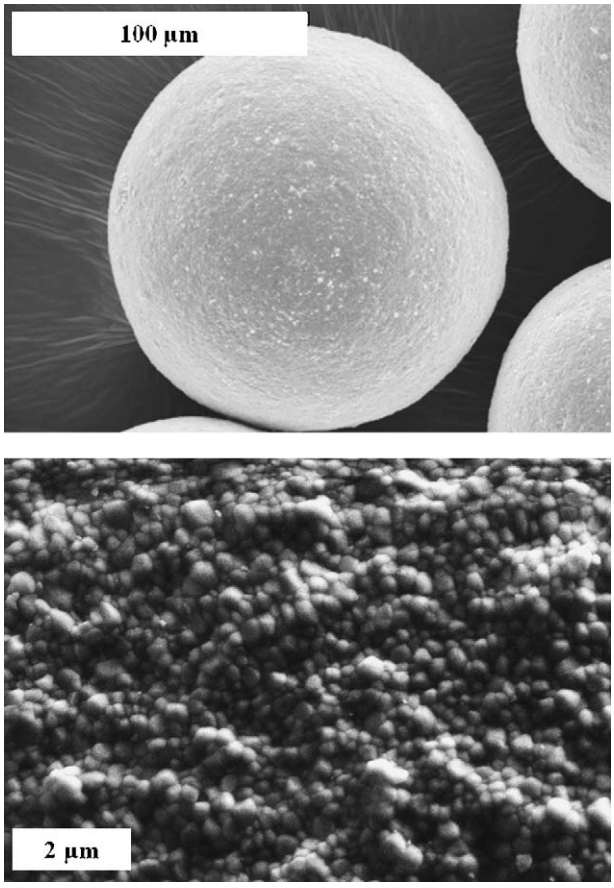

Fig. 3. SEM micrographs of the ZrO_2 abrasive particles.

The samples were polarized to a fixed potential (2 V HESS, hydrogen electrode same solution) to ensure well-defined oxide conditions. After loading the particles the system was sealed and the experiment was started. The recorded transients were subsequently analyzed in order to determine the main characteristics of the repassivation process:

- peak current (I_{max}),
- time of peak current ($=t_0$),
- current rise time (I_{rise}),
- repassivation time (Δt),
- charge consumed (Q),
- background current (I_{back}).

By reducing the amount of particles introduced into the system for each experiment it was possible to achieve a single impact on each sample while simultaneously recording the corresponding transient for each impact. The evaluation of the transient data in combination with the subsequent *ex-situ* scanning electron microscope (SEM) investigations allows a correlation of the obtained electrochemical data with the physical damage and wear experienced by each sample.

3. Results

Using the technique described above single-impact transients were recorded at the impingement angles of 90°, 60°, 45° and 30°. The recorded transients are shown in Fig. 4.

The charge consumed during repassivation was determined by numerical integration. As described in detail in [14] the repassivation of Al under these conditions should require times in the range of 100 s. The acquired transients show that the current recedes back to the initial background level in well under 1 s. Therefore an additional determination of the charge was performed. This was done by finding the linear part of the double-logarithmic plot of the transient and extrapolating this linear current decay for 100 s. Subsequent integration of this (extrapolated) transient yields a better measure of the true repassivation current. The results are given in Table 2. Additionally the amount of newly formed oxide $n(Al_2O_3)$ was calculated from the obtained values for the repassiviation charge. Using these values it was also possible to determine the volume $V(Al_2O_3)$ of newly formed oxide and – taking into account the precisely defined oxide thickness – the repassivated surface area $A_{ox}(Al_2O_3)$. Details are given below.

The crater dimensions were determined from the SEM imagery and the crater surface was calculated using the standard equation, where a and b are the crater axes:

$$A_{crater} = \frac{\pi}{4}ab \quad (2)$$

This equation gives the euclidic surface area. The fact that the indent crater is actually bowl-bottom-shaped gives rise to the calculation of the increase in surface caused by the impacting

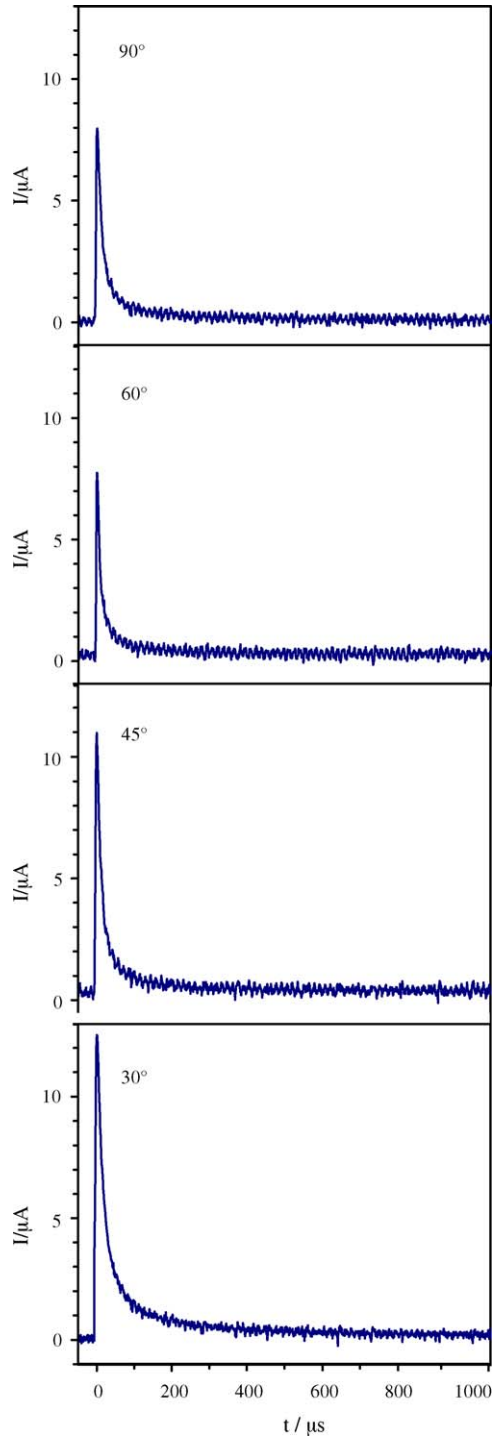

Fig. 4. Repassivation transients at different impingement angles.

particle. As the depth of indentation is very small compared to the crater diameter (∼3%) this increase can be neglected. Therefore Eq. (2) was used to calculate the crater surface area. Since all experiments were performed under potentiostatic conditions (2 V HESS) the thickness of the oxide layer can be precisely determined using Eq. (3) where ΔE is the difference between the applied potential and the oxide formation potential E_0 for the given oxide – in the case of aluminium E_0 equals −1.6 V HESS – and $k = 1.6\,\mathrm{nm\,V^{-1}}$ is the oxide growth factor [15]:

$$d_{ox} = \Delta E k = (2\,\mathrm{V} + |-1.6|\ \mathrm{V})1.6\,\mathrm{nm\,V^{-1}} = 5.76\,\mathrm{nm} \quad (3)$$

With the known oxide thickness and the application of Eq. (4) the repassivated surface area A_{ox} can be derived [15]:

$$A_{ox} = \frac{Q M_V}{z F d_{ox}} \quad (4)$$

Q is the charge obtained through numerical integration of the recorded transient, M_V the molar volume of the oxide, z the number of electrons passed per formula unit (Al_2O_3) of oxide and F is the Faraday constant. Fig. 5 shows the SEM micrographs corresponding to the transients in Fig. 4.

As can be seen in Fig. 5 the impact crater morphology changes with impingement angles. The impact crater caused under perpendicular impingement is nearly perfectly round, whereas the impact craters at lower angles are elongated and show scratch marks. This scratching is a result of the nano-roughness of the ZrO_2 particles (Fig. 3). At very low angles a pile-up of material is observed. This indicates a change of the wear mechanism.

Fig. 6 shows the results of the electrochemical data evaluation. There is a definite trend to higher damaged surface areas at ever decreasing impingement angles. The same trend is seen when plotting the extrapolated charge.

Table 2
Determination of depassivated surface area from the consumed charge with and without extrapolation of the current transient

Angle/°	Q/nC	$n(Al_2O_3)$ /amol	$V(Al_2O_3)$ /$\times 10^{-20}$ m^3	$A_{ox}(Al_2O_3)$ /µm^2
Without extrapolation				
90	0.34	0.58	1.51	2.89
60	0.30	0.51	1.33	2.55
45	0.55	0.95	2.44	4.68
30	0.80	1.38	3.55	6.81
With extrapolation				
90	1.08	1.87	4.81	9.23
60	0.83	1.44	3.70	7.10
45	1.26	2.17	5.58	10.70
30	2.21	3.82	9.81	18.83

4. Discussion

The damage to the µ-electrodes was assessed as described above. As can be seen in Table 2 the crater surface areas range from 200 to 300 µm^2, whereas the depassivated surface area – the amount of surface area that was repassivated after impingement – is between 2 and 7 µm^2. Obviously, the crater is not completely depassivated on impact, rather the oxide is cracked and/or pierced by the impacting particle. At lower angles scratching contributes an additional component to the total amount of wear (Fig. 7). As depicted in Fig. 6 the amount of scratching is dependent on the impact angle: upon perpendicular impingement the impacting particle rebounds from the sample surface leaving a round impact crater. At an angle of 60° the amount of scratching is very low; the largest scar was obtained after impingement at an angle of 45° (Fig. 5). At very low impingement angles the crater

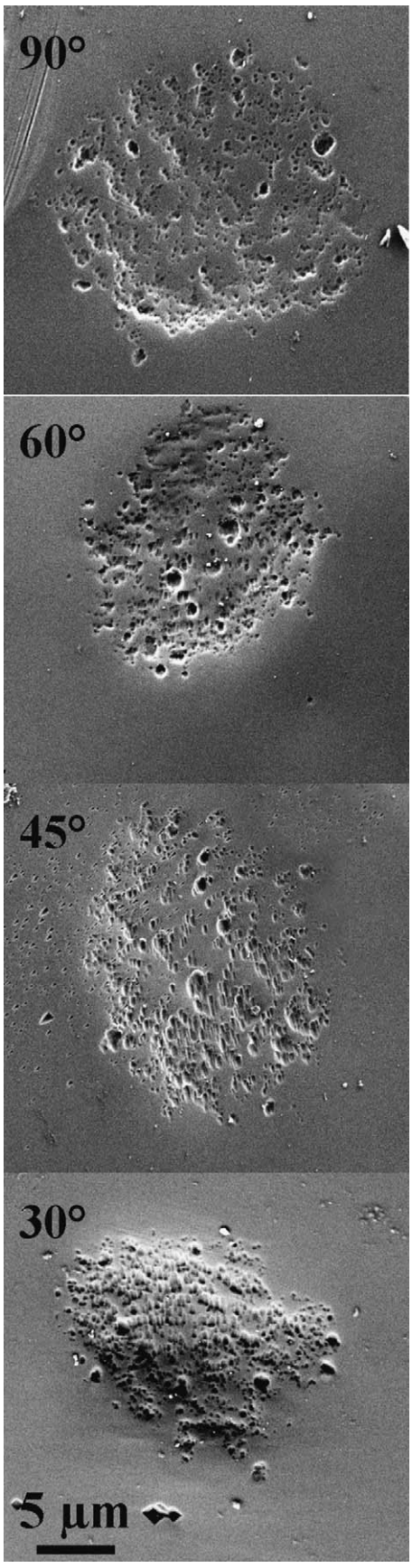

Fig. 5. SEM micrographs of the impact craters corresponding to the transients shown in Fig. 4.

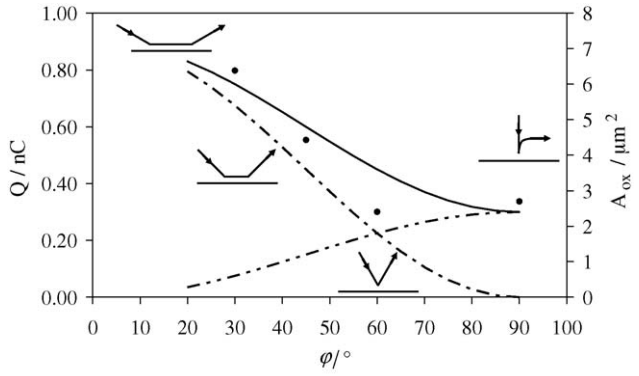

Fig. 6. Evaluation of electrochemical data; obtained charge from numerical integration and repassivated surface area from Eq. (4); the dots represent the measured data points, the solid line shows the results of the approximation using Eq. (8), the dashed lines depict the individual components ((- ⋯ -) normal; (- · -) lateral) of the damage caused by the impacting particle.

size is reduced, but there are indications of material pile-up due to the softness of the sample material.

As indicated in the upper part of Fig. 1 the impact of the sphere can be divided into two components: the impacting momentum in normal direction and the scratching motion in the lateral direction. Using Eq. (5) the kinetic energy E_{kin} of the impacting particle can be derived from the impulse $p = mv$ and the particle mass:

$$E_{\text{kin}} = \frac{p^2}{2m} \tag{5}$$

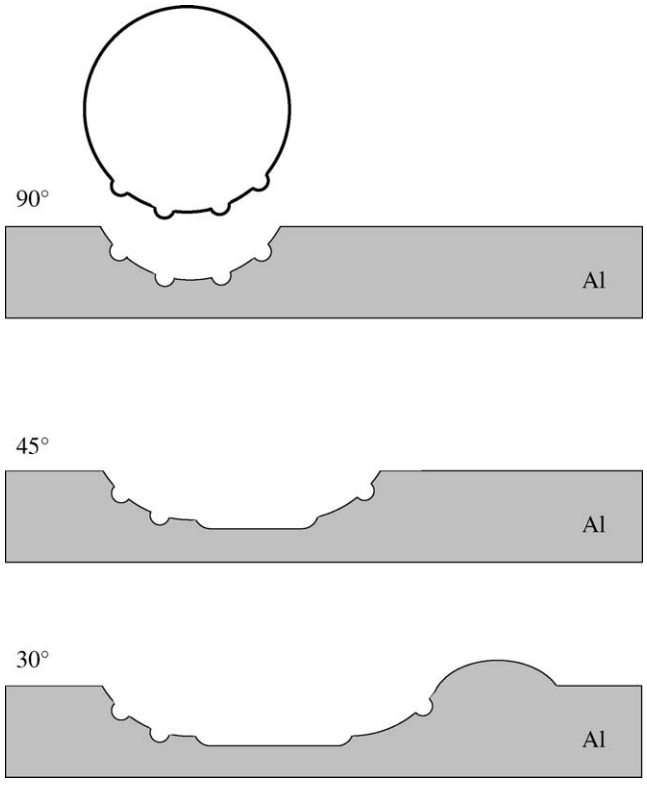

Fig. 7. Model of material deformation upon impingement attack.

The separation of the normal and lateral components is achieved in Eqs. (6) and (7):

$$E_{\mathrm{kin\_n}} = \frac{p_{\mathrm{n}}^2}{2m} = \frac{1}{2} m \sin^2 \varphi v^2 \tag{6}$$

where $E_{\mathrm{kin\_n}}$ is the kinetic energy in the normal direction, p_{n} the impulse in normal direction, m the particle mass, φ the impingement angle and v is the particle velocity.

$$E_{\mathrm{kin\_l}} = \frac{p_{\mathrm{l}}^2}{2m} = \frac{1}{2} m \cos^2 \varphi v^2 \tag{7}$$

where $E_{\mathrm{kin\_l}}$ is the kinetic energy in the lateral direction and p_{l} is the impulse in lateral direction.

Obviously there is a connection between the kinetic energy of the impacting particle and the damage caused on the sample surface. The damage can be quantified by determining the consumed charge as is shown in Table 2. Therefore a correlation of Eqs. (6) and (7) was achieved by formulating Eq. (8) while adding the coefficients i and s to describe all the experimental factors such as particle mass, particle velocity and the connection between kinetic energy and consumed charge:

$$Q = i \sin^2 \varphi + s \cos^2 \varphi \tag{8}$$

The curve obtained from Eq. (8) is plotted as the solid line in Fig. 6; the individual components are also given as dotted lines in Fig. 6: $Q = i \sin^2 \varphi$ as (-··-) and $Q = s \cos^2 \varphi$ as (-·-). The values determined for the coefficients by curve fitting are $i = 0.3$ and $s = 0.9$.

It must be mentioned that the formulas given above are not based on a strict kinetic model, rather they are obtained through a comparison of the involved components. Apparently the kinetic energy of the impacting particle activates two different wear mechanisms: the first being indentation, the second being scratching. The lateral and normal components are attributed to either of these mechanisms.

The difference of the values of i and s indicate the necessity of a different description of the underlying processes. A more detailed investigation with more measurements at each impingement angle at various impact angles, as well as a variation of other experimental parameters (particle mass, particle velocity, particle surface morphology) should yield data, allowing a more detailed kinetic description of the wear mechanisms.

Acknowledgement

A.J. Smith acknowledges the financial support of the Max-Buchner-Stiftung through a Max-Buchner-Forschungsstipendium.

References

[1] D. Landolt, S. Mischler, M. Stemp, Electrochim. Acta 46 (2001) 3913.
[2] D. Landolt, S. Mischler, M. Stemp, S. Barril, Wear 256 (2004) 517.
[3] F. Assi, H. Böhni, Wear 235 (1999) 505.
[4] M. Matsumura, Y. Oka, H. Hiura, M. Yano, Isij Int. 31 (1991) 168.
[5] J. Li, Y.G. Zheng, J.Q. Wang, Z.M. Yao, Z.F. Wang, W. Ke, Wear 186 (1995) 562.
[6] Y.G. Zheng, Z.M. Yao, X.Y. Wei, W. Ke, Wear 186 (1995) 555.
[7] A.M. Fan, J.M. Long, Z.Y. Tao, Wear 193 (1996) 73.
[8] J.B. Zu, I.M. Hutchings, G.T. Burstein, Wear 140 (1990) 331.
[9] G.T. Burstein, K. Sasaki, Wear 240 (2000) 80.
[10] Y. Li, G.T. Burstein, I.M. Hutchings, Wear 186 (1995) 515.
[11] G.T. Burstein, K. Sasaki, Electrochem. Acta 46 (2001) 3675.
[12] G.T. Burstein, A.J. Davenport, J. Electrochem. Soc. 136 (1989) 936.
[13] G.S. Frankel, B.M. Rush, C.V. Jahnes, C.E. Farrell, A.J. Davenport, H.S. Isaacs, J. Electrochem. Soc. 138 (1991) 643.
[14] A.W. Hassel, A.J. Smith, Corros. Sci. (in press).
[15] A.W. Hassel, Elektronische und Ionische Transportprozesse in ultradünnen Ventilmetalloxidschichten, PhD thesis, Shaker Verlag, Aachen, 1997.